

Learning Elastic Constitutive Material and Damping Models

Bin Wang Paul Kry Yuanmin Deng Uri Ascher Hui Huang Baoquan Chen

Abstract—The fidelity of a deformation simulation is highly dependent upon the underlying constitutive material model. Commonly used linear and nonlinear constitutive material models contain many simplifications and only cover a tiny part of possible material behavior. In this work we propose a framework for learning customized models of deformable materials from sparse example surface trajectories. The key idea is to iteratively improve a correction to a nominal model of the elastic and damping properties of the object, which allows new forward simulations with the learned correction to more accurately predict the behavior of a given soft object. The challenge is that such data is sparse as it is typically available only on part of the surface. Sparse reduced space-time optimization identifies gentle control forces with which we extract necessary annotated data for model inference and to finally encapsulate the material correction into a compact parametric form. We demonstrate our method with a set of synthetic examples, as well as with data captured from real world homogeneous elastic objects.

Index Terms—Computing methodologies, physical simulation, elastic and damping model, dynamics

1 INTRODUCTION

THE simulation of deformable objects is ubiquitous in computer graphics and robotics research due to the large number of varied applications, including animation, movie making, medical treatment and manufacturing. To obtain accurate deformation simulation, finite element modelling and continuum elasticity laws are typically employed, where a constitutive material model that can cover the range of material behavior is selected. Subsequently, the material parameters are needed to be carefully tuned in order to fit empirical data. Data driven based methods have recently exhibited great potential in this direction. Advanced scanning technologies can be used to faithfully capture a deformation behavior under external force, and in turn the data can be used to estimate the parameters of the mathematical model.

However, currently there is no standard solution for choosing appropriate constitutive models, especially for large deformations, real-world material modelling, fine level simulation of heterogeneous models, and artist designed cartoon physics. The situation for modelling damping is even worse. Indeed, there is no agreement about damping model in the mechanical engineering literature which can describe various damping effects in a unified way. Many use the Rayleigh model, but it can be inadequate for visual purposes [1]. Based on these observations, in this paper

we propose a more general material inference framework obtained by directly learning constitutive laws rather than fitting parameters. Similar ideas have also been used by [2] and [1], which focus on providing a forward modeling tool for material design. Learning a constitutive model is challenging because: (1) the model should be able to encapsulate all the variations of material properties in a generic way; (2) there may be no obvious source of training data.

The main contribution of this paper are:

(1) The constitutive material model is designed as a combination of empirical baseline model and a parametric representation, in which all the variations of material properties are encapsulated. This model maintains a good balance between stability and flexibility.

(2) We propose a progressive inverse learning framework, which is capable to learn a complex constitutive material from sparse motion trajectories. The highlight in this framework is leveraging a space-time optimization technique to generate annotated data for constitutive model fitting.

(3) By incorporating a probabilistic correspondence representation, a differentiable shape matching metric is developed. Significantly, this allows our system to work faithfully on real-world captured data.

Fig. 1 shows a preview of our approach and results. We demonstrate the performance of our approach on several problems, including synthetic examples, coarsening applications, and captured data. The variety of results described in Section 7 leads us to conclude that we have achieved an important step towards the data based construction and understanding of nonlinear constitutive elastodynamic force models.

- *Bin Wang is with Advanced Innovation Center for Future Visual Entertainment of Beijing Film Academy. E-mail: binwangbuaa@gmail.com*
- *Paul Kry is with School of Computer Science, McGill University. E-mail: kry@cs.mcgill.ca*
- *Yuanmin Deng is with School of Computer Science and Technology, Shandong University. E-mail: yuanmin.deng@gmail.com*
- *Uri Ascher is with Department of Computer Science, University of British Columbia. E-mail: ascher@cs.ubc.ca*
- *Hui Huang is with College of Computer Science and Software Engineering, Shenzhen University. E-mail: hhzhiyan@gmail.com*
- *Baoquan Chen is with Advanced Innovation Center for Future Visual Entertainment of Beijing Film Academy and Peking University. E-mail: baoquan.chen@gmail.com*
- *Hui Huang and Baoquan Chen are the corresponding authors of this paper.*

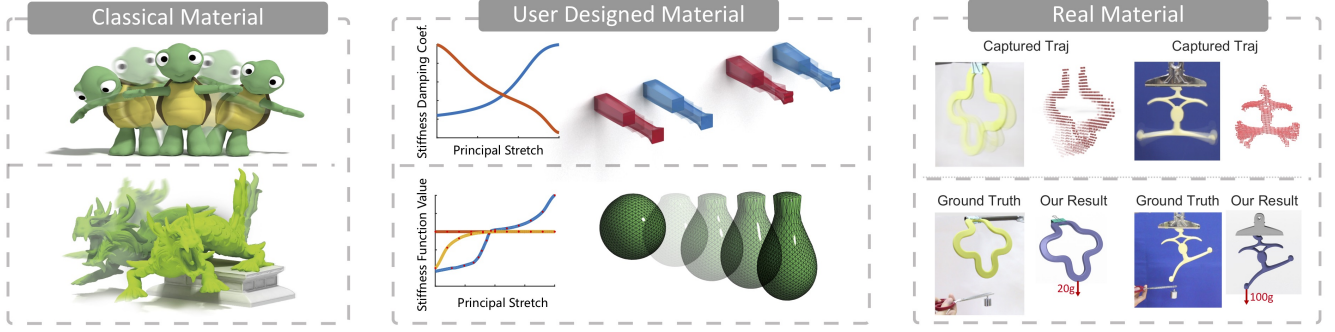


Fig. 1: Our parametric material model learns a correction to a nominal material model from kinematic data alone, allowing us to accurately capture the nonlinearity of different constitutive material models. Left: classical nonlinear constitutive material. Middle: user designed elasticity and damping. Right: real world material.

2 RELATED WORK

2.1 Data Driven Based Deformation Modeling

With recent improvements in sensing technologies, the data-driven approach of modeling and reconstructing deformation parameters from real world measurements has offered great potential for computer graphics applications, such as fabrics, soft objects, and human organs and faces [3], [4], [5], [6], [7], [8]. Bickel et al. [8] fit material parameters with an incremental loading strategy to better approximate nonlinear strain-stress relationships. Wang et al. [6] proposed a piecewise linear elastic model to reproduce nonlinear, anisotropic stretching and bending of cloth. Miguel et al. [7] directly optimized nonlinear stress-strain curves based on measurements. Then Miguel et al. [9] estimated internal friction. Further, Miguel et al. [10] developed a method for modeling example based materials with energy functions for both cloth and elastic solids.

A common limitation with previous methods is that they require a dense force displacement field. While Bhat et al. [11] avoided the need for force capture by using video tracking of cloth, they still assumed a trivial cloth reference shape. Yang et al. [12] presented a learning-based algorithm to recover material properties of cloth from videos, using training data sets generated by physics-based simulators, and their focus was on material type estimation due to inconsistency between real and synthetic data and sparse material space sampling. Davis et al. [13] estimated material and damping properties through extracting small vibration mode from high-speed and regular frame-rate video. Wang et al. [14] estimated linear elastic material parameters from partially observed surface trajectories of an object's passive dynamics. Our work has a similar setting, but focuses on correcting the errors that arise from assuming simple elastic and damping force models.

2.2 Material Design

Another popular trend in computer graphics is to directly fit parametric functions as a material description. Xu et al. [2] provided a method to design isotropic and anisotropic (orthotropic) nonlinear solid elastic materials using a piecewise spline interface, which can provide local control on deformation behavior. A hyperelasticity model based on energy addends proposed by [10] allows modelling of various nonlinear elasticity effects in a separable manner. Instead of

explicitly modelling the stress-strain relationship, Martin et al. [15] and Schumacher et al. [16] promoted an art-directed approach to solid simulation, which constructs a manifold of preferred deformations by examples and guides the object towards it. Coarsening techniques have proved useful for computational design for fabrication [17], [18], [19], where one must deal with the problem of creating equivalent physics based models. Kharevych et al. [20] took an energy based approach to coarsening composite elastic objects through the use of global harmonic displacements. Nesme et al. [21] created nonlinear shape functions and projected fine-level mass, stiffness, and damping matrices to produce coarse composite elements, while Torres et al. [22] introduced an improved element based coarsening method that deals with co-rotation. Compared with elasticity modelling, few publications have focused on the design of damping model, the work of [1] being the first to present a design method for anisotropic and/or nonlinear damping effects. Banderas et al. [23] focuses on dissipation potentials based damping modelling, similarly to us using strain rate to control damping. Targeting cloth hysteresis effects, Miguel et al. [9] proposed a internal friction model based on an augmented reparameterization of Dahl's model.

In our work, inspired by [2] we use principal stretches to formulate nonlinear elastic and damping force corrections due to its complexity and flexibility. However, instead of using a spline interface, we adopt RBF and NN representations to parameterize the material correction.

2.3 Machine Learning in Material Science

NN analysis has had a liberating effect on materials science, by enabling the study of incredibly diverse phenomena which are not as yet accessible to physical modelling [24], [25]. Jung and Ghaboussi [26] modeled rate-dependent materials with NN, giving results both for a synthetic example and for data from a pre-stressed concrete beam. Stefanos and Gyan [27] used the length of strain trajectory traced by a material point, also called intrinsic time, as an additional input parameter in training. This is essential for situations of cyclic and transient loading. To overcome the challenge of training a convolutional NN with a small dataset, Liang et al. [28] employed a training strategy that combines three key ideas: unsupervised deep learning to determine the filter parameters of a convolution layer (generally using encoder-decoder

based unsupervised learning strategies), supervised learning to determine the parameters in the classifier or regressor layer, and data augmentation to generate more training data. In the computer graphics community, deep learning technology for deformation modelling has gradually gained more attention. The DeepWarp technique of [29] attempts to learn a mapping from a linear elasticity simulation to its nonlinear counterpart. Fulton et al. [30] perform time integration of the elastodynamic system in a learned nonlinear reduced latent-space, which is represented using an artificial NN. In comparison, the algorithm proposed in our paper puts emphasis on how to accurately approximate the underlying constitutive model for FEM simulation. We will demonstrate that traditional computer graphics algorithms can be adapted to address an interesting and timely problem involving data labeling and augmentation.

3 OVERVIEW

The core of our approach is to learn accurate elastic and damping properties of an object through trajectory fitting. A baseline constitutive elastodynamic model, called nominal model in Fig. 2, is assumed to be given. The inferred baseline model correction is encapsulated in RBF or Neural Network parametric representation.

The input of the system is a set of incomplete surface trajectories of an object moving dynamically, unforced, in response to an initial perturbation. The main loop alternates between solving a sparse reduced space-time optimization problem, and fitting a correction function (see Fig. 2). The sparse reduced space-time optimization softly constrains nodes of the tetrahedral mesh to follow a sparse collection of incomplete surface trajectories in addition to the discretized physical equations of motion. Through injecting gentle forces we can keep the system trajectories close to desired input trajectories and still obey Newton’s physical laws. The key idea is that this gentle control force identifies what is currently missing due to material model inaccuracy and should be compensated using the correction model. Additionally, we solve an overdetermined problem to identify the missing corrective stress on each tetrahedron from the vertex control forces taking all the frames into consideration. Then, the best fit correction model is distilled from the strain, strain rate, and stress data. In the following iterations, the current correction of the nominal material model is added to both the forward simulation and the space-time optimization. As the iterations progress, the correction is gradually refined to provide better accuracy, which in turn improves how the forward simulation matches the example trajectory. During each optimization iteration, the correction is encapsulated in an RBF parametric representation, and it is only after the final iteration that we train a compact NN based representation with data sampled from the final RBF function.

At the beginning of each iteration, we complete a forward simulation with the updated material model to evaluate how well this trajectory matches the example surface trajectory to determine convergence. We can similarly monitor the magnitude of gentle control forces identified by the space-time optimization at each loop, and continue to iterate as long as we see improvement, even if the forward

simulation error alone does not reveal that progress is being made. We also use this regular forward simulation trajectory to extract a reduced basis for the optimization. Moreover, We compute an initial seed trajectory for this simulation using a forward simulation, which includes constraints on the immobilized parts of the mesh, as well as constraints to ensure that the trajectories of the sparse surface points follow their known positions. The constrained forward simulation gives a good starting point for the sparse reduced space-time optimization, which quickly converges to a solution that identifies a plausible trajectory for unobserved nodes and the corresponding gentle control forces.

4 MATERIAL MODEL

Even though there are plenty of empirical hyperelastic constitutive material models such as the nonlinear St. Venant-Kirchhoff, neo-Hookean, Ogden or Mooney-Rivlin materials, they do not account for all deformation phenomena that may arise. Choosing a correct model to fit measurement data is already a difficult task. Our data-driven approach allows us to learn a parametric material model that can encapsulate a wide range of elastic and damping properties in a compact and unified correction function.

4.1 Nominal Material Model and Assumptions

Our deformable models are constructed using linear shape functions. In order to handle large deformations of soft objects, the nominal material is described in terms of the widely adopted co-rotated linear FEM, formulated using principal stretches [2]. The ensuing computation of the element stresses and vertex forces is straightforward.

The deformation gradient F for each tetrahedron is diagonalized by SVD, $F = U\hat{F}V^T$, and the first Piola-Kirchhoff stress is computed with the principal stretches, $\hat{P}(\hat{F}) = 2\mu(\hat{F} - I) + \lambda\text{tr}(\hat{F} - I)I$ where μ and λ are Lamé parameters. The diagonal stress is then transformed back to the world frame, $P = U\hat{P}(\hat{F})V^T$. An element’s contribution to its vertex forces is PB_m , where B_m is the inverse material space shape matrix (see [31]). Summing the contribution of all elements, we can build a large sparse matrix B , which combines the entries in U , V , and B_m , and can be multiplied by the block vector of all element diagonal stresses \hat{p} to give a block vector of all vertex forces f , that is, $B\hat{p} = f$.

We also include Rayleigh damping in our nominal model, with forces computed by $(\alpha_0M + \alpha_1K)\dot{x}$, where \dot{x} are the FEM vertex velocities, M is the lumped mass matrix, and K is the stiffness matrix assembled from per-element stiffness matrices. The nominal model parameters are assigned manually or computed with the method of [14].

4.2 Parametric Material Correction Model

Our parametric material correction model ultimately computes a correction to the Piola stress to compensate for the elasticity and damping simultaneously. Similar to [32], the stress correction is computed in a rotated frame from diagonalized strain and strain-rate as $\Delta\hat{P} = N(\hat{F}, \dot{F})$, and then rotated back to current world frame by the same U and V used to diagonalize F . Here, \dot{F} is defined as the 3

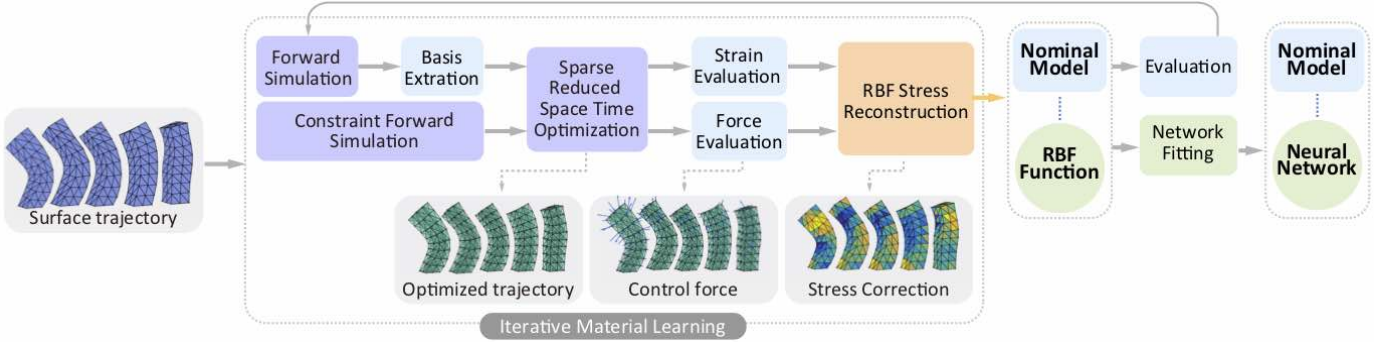


Fig. 2: Schematic overview of our data-driven parametric material learning framework which iteratively learns a correction to a nominal material model that allows us to accurately reproduce the captured trajectory, even when the nominal model differs significantly.

diagonal components of $U\dot{F}V^T$, where \dot{F} is the deformation gradient velocity. Using principal stretches and the diagonal deformation gradient velocity reduces the complexity of our function approximation problem, but still permits complex stress corrections and strain dependent damping.

As discussed later, the 6-input 3-output function approximation problem allows us to use an RBF with a moderate number of basis functions, and select a network architecture with a moderate number of hidden nodes. The corrected stresses in the world frame are

$$P_n = U(\hat{P}(\hat{F}) + N(\hat{F}, \hat{F}))V^T. \quad (1)$$

For implicit integration, the gradient of N can be easily computed from the RBF, or from the NN function with automatic differentiation; the gradient of stress P with respect to the deformation gradient F can be computed by the product rule and a careful evaluation of the different terms [2].

5 FORCE CORRECTION ESTIMATION

The desired surface trajectory provides a rich source of information about the dynamics of the object. The purpose of using space-time optimization is to compute a set of gentle control forces that will drive the simulation follows captured data. Consequently, necessary information to correct our currently estimated parametric material model such that the simulation follows captured data can be distilled from space-time optimization result.

5.1 Sparse Reduced Space-Time Optimization

Many variations of the space-time constraints approach of [33] have been proposed. To deal with the large number of degrees of freedom in our deformable models, we use reduction and sparse constraints taking inspiration from [34] and [35].

We compute a reduce basis Φ using a data driven based method Proper Orthogonal Decomposition(POD), which perform principal component analysis (PCA) on forward simulation trajectory with the provided initial conditions and our current approximation of the material model. For the analysis we use a short portion of the forward simulation sequence which targets the most interesting dynamics, and perform PCA on only a fraction of the frames, in turn keeping only a fraction of the vectors for the basis.

We solve the space time optimization as an error minimization problem with an objective function that consists of two parts: physical error, and sparse trajectory error. Using a discretized approximation of the acceleration, the unreduced equation of motion at time step i is given by

$$h^{-2}M(x_{i-1} - 2x_i + x_{i+1}) = B_{i+1}p_{n,i+1} + f_{ext}, \quad (2)$$

with gravity force f_{ext} . This equation corresponds to our forward integration method because the force term evaluation is at the end of the time step. However, we optimize with reduced coordinates z_i , where $x_i = \Phi z_i$, thus, the reduced physics errors at each time step are

$$C_f \equiv h^{-2}\Phi^T M \Phi (z_{i-1} - 2z_i + z_{i+1}) - \Phi^T B_{i+1} p_{n,i+1} - \Phi^T f_{ext}. \quad (3)$$

The desired example trajectory is sparse because it comes from an incomplete scan of the surface. Letting vector s_i contain the desired point positions at time step i , we can write the sparse trajectory error at each time step as

$$C_{zi} \equiv \lambda(S\Phi z_i - s_i), \quad (4)$$

where the wide sparse selection matrix S extracts the components of the desired positions by having one non-zero entry per row. The scalar λ is used to specify the weight of position constraints given that the combination of physics and position constraints are solved in a soft manner.

Letting $\mathbf{C}(z)$ concatenate all physics errors \mathbf{C}_f on top of all position errors \mathbf{C}_{zi} , our goal is to find a reduced trajectory z that minimizes the violation of both, that is, minimizes $\|\mathbf{C}\|^2$. We solve this using standard techniques. We do not assemble the Jacobian matrix $\frac{\partial \mathbf{C}}{\partial z}$ directly, but use the chain rule and keep it in the factored form $\frac{\partial \mathbf{C}}{\partial x} \frac{\partial x}{\partial z}$, where $\frac{\partial x}{\partial z}$ simply contains copies of the basis matrix Φ . The matrix $\frac{\partial \mathbf{C}_f}{\partial x}$ has a very simple part that links vertices at different time steps through the acceleration term, and a more complex part where the chain rule must be applied to compute the force gradient. This would normally include a contribution from the parametric material correction, but generally we note better convergence when we omit it, leaving only the gradient of the nominal material. Because we still have the parametric material correction on the right hand side, we only change the convergence and not the solution. Thus, this second part sprinkles off diagonal terms into the matrix linking vertices that are adjacent to a common element. The matrix $\frac{\partial \mathbf{C}_{zi}}{\partial x}$ simply contains copies of the selection matrix S .

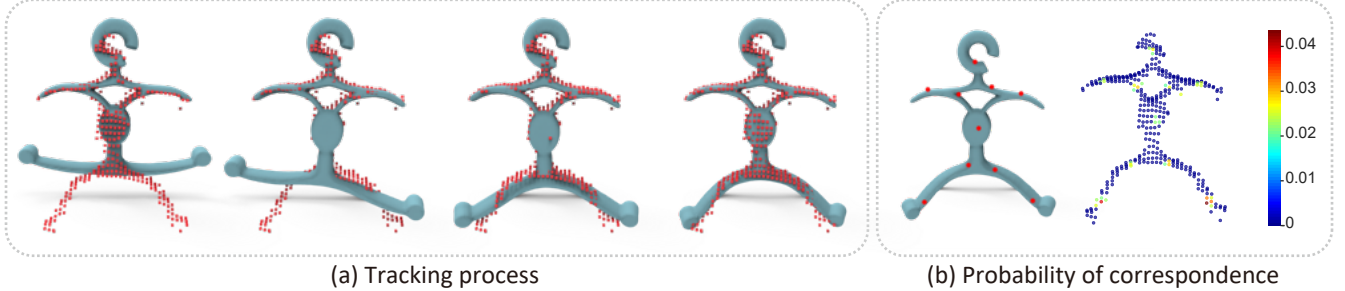


Fig. 3: Point cloud tracking and shape similarity matching: (a) the physics-based probabilistic tracking method gradually deforming the mesh to fit the point cloud; (b) the final maximum correspondence for each point in the point cloud to a selection of 10 surface points, which shows tight localized correspondence between the point cloud and the selected points.

While the Jacobian matrix is very large, it is also very sparse. We compute the solution using the CUSP [36] library’s sparse least square conjugate gradient implementation on GPU.

We can check for convergence to solution \mathbf{z}^* by monitoring our progress in reducing the violation of physics errors in Equation 3. Once converged, it is exactly these violations that provide the necessary control forces to refine our current parametric material correction model. That is, given an optimized reduced trajectory \mathbf{z} , the gentle control force is computed as

$$\mathbf{f}_{i+1} = h^{-2} \mathbf{M} \Phi(\mathbf{z}_{i-1} - 2\mathbf{z}_i + \mathbf{z}_{i+1}) - \mathbf{B}_{i+1} \mathbf{p}_{n,i+1} - \mathbf{f}_{ext}. \quad (5)$$

While it may be desirable to solve for control stresses at each element, as these are what is required for learning a correction, our approach permits an easier solution that directly provides a control force at each vertex.

5.2 Constrained Forward Simulation

The sparse reduced space-time optimization needs a reasonable starting trajectory. While the forward simulation with the current parametric material correction could serve this purpose, we find it valuable to simulate a trajectory that is also constrained to follow the desired surface motion. For the forward simulation, we solve at each step the equation

$$\mathbf{A} \Delta \mathbf{v} = h \mathbf{f}, \quad (6)$$

where $\mathbf{f} = \mathbf{B} \mathbf{p}_n + \mathbf{f}_{ext}$, with \mathbf{p}_n being the block vector of stress corrections at the current time step and \mathbf{f}_{ext} the external gravity force, and $\mathbf{A} = \mathbf{M} - h\mathbf{D} - h^2\mathbf{K}$, where \mathbf{D} and \mathbf{K} are assembled using the gradient of Equation 1. Many of our models are rigidly attached to the world, and we typically remove these degrees of freedom from the system. We can further divide the vertices into two groups,

$$\begin{pmatrix} \mathbf{A}_{uu} & \mathbf{A}_{uc} \\ \mathbf{A}_{cu} & \mathbf{A}_{cc} \end{pmatrix} \begin{pmatrix} \Delta \mathbf{v}_u \\ \Delta \mathbf{v}_c \end{pmatrix} = h \begin{pmatrix} \mathbf{f}_u \\ \mathbf{f}_c \end{pmatrix}, \quad (7)$$

where we use subscripts u for unconstrained and c for constrained. The second block row can be discarded leaving us a smaller system to solve, namely,

$$\mathbf{A}_{uu} \Delta \mathbf{v}_u = h \mathbf{f}_u - \mathbf{A}_{uc} \Delta \mathbf{v}_c. \quad (8)$$

Here, $\Delta \mathbf{v}_c$ at time step i is computed by a second order central finite difference, $h^{-1}(x_{i-1} - 2x_i + x_{i+1})$. We solve these large sparse systems using PARDISO [37], [38].

5.3 Space-time Optimization on Noisy Real Data

For real material observations, the real world data can be incomplete (i.e., only partial surface scans), can be noisy, and can be in the form of unparameterized point clouds. Thus, the exact desired point positions s_i at each time step i needed in Equation 4 are no longer available. We must modify the trajectory error in the space time optimization to adaptively match nodes of the tetrahedral mesh when they are close to the surface scans. We do this for every iteration for finding \mathbf{z}^* in a manner which is inspired by the physics-based probabilistic tracking method proposed by [39] and extended in [14].

For a frame consisting of N points at a given time instant (time step i), we denote point coordinates in the point cloud by \mathbf{c}_n for $n = 1 \dots N$, and vertex positions in the surface mesh by \mathbf{s}_k for $k = 1 \dots K$. Let the probability of correspondence between the point cloud and the mesh vertices be p_{kn} . Assuming that \mathbf{c}_n is normally distributed around \mathbf{s}_k as $\mathbf{c}_n \sim \mathcal{N}(\mathbf{s}_k, \Sigma_k)$ with an isotropic covariance matrix $\Sigma_k = \sigma^2 \mathbf{I}$, then we compute the probability that nodal value \mathbf{s}_k of the surface mesh corresponds to the observation \mathbf{c}_n as

$$p_{kn} = \frac{1}{\sqrt{(2\pi)^3 \|\Sigma_k\|}} \exp \left(-\frac{1}{2} (\mathbf{c}_n - \mathbf{s}_k)^T \Sigma_k^{-1} (\mathbf{c}_n - \mathbf{s}_k) \right).$$

Note that parameter σ is set based on the accuracy of the scanner. We only assign point \mathbf{c}_n to \mathbf{s}_k if there is a large probability (i.e., we truncate p_{kn} to zero if the value is below a threshold). Fig. 3 shows how the mesh gradually conforms to point cloud data, along with final probabilities of correspondence between the point cloud and selected example vertices.

Now, we can reformulate the trajectory constraints of Equation 4 as a weighed distance between each vertex and its corresponding patch of point clouds as

$$\mathbf{C}_{zi} \equiv \lambda \sum_{k,n} p_{kn} \Sigma_k^{-1} (\mathbf{c}_n - \Phi_k \mathbf{z}_i), \quad (9)$$

where Φ_k gives the position of surface point k from reduced coordinates \mathbf{z}_i , i.e., $\mathbf{s}_k = \Phi_k \mathbf{z}_i$. The Jacobian matrix required for space-time optimization of this modified position error is straightforward to compute.

During space-time optimization, the correspondence probability between point cloud and mesh surface is updated, which allows the mesh nodes to move freely across

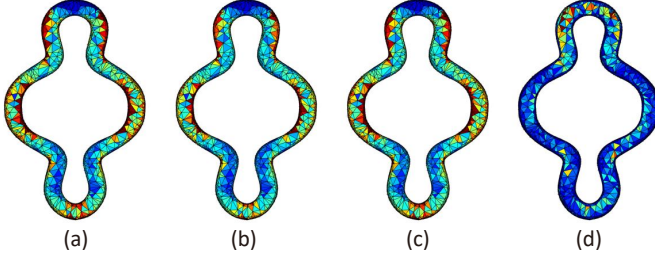


Fig. 4: Von Mises stress visualization for comparison of reconstruction results from given nodal elastic forces. The pot holder with neo-Hookean material is deformed due to external load. (a) Ground truth. (b) RBF based reconstruction result with 40 kernels. (c) RBF based reconstruction result with 80 kernels. (d) Least squares reconstruction result.

on the point cloud surfaces. This manner of building parameterized surface trajectories effectively uses the point cloud data as a soft constraint on the nominal model, and permits reasonable estimate of surface node trajectories.

We use a very similar approach for building the initial starting point for space time optimization from real data. The tracking procedure in Fig. 3 clearly demonstrates that the mesh can well track the point cloud data even in the presence of large discrepancies.

6 PARAMETRIC MATERIAL CORRECTION

The strain and strain-rate trajectory from the space-time optimization, combined with the vertex control forces, cannot be directly used for function fitting. First of all, the control forces are defined on each vertex, which is highly related with the topology. Moreover, the gentle control forces may not be entirely self-consistent (i.e., an element might need different forces to correct a given state of strain and strain-rate at different parts of the trajectory). Finally, the amount of data derived from optimization is quite limited. In this section, we describe how we use two complementary parametric representations to fit the model.

6.1 Stress Reconstruction from Nodal Force

Section 4.1 introduced the equation $B\hat{p} = f$, which relates element stresses to nodal forces. We can compute the stresses as an underdetermined least squares problem using LSQR [40], which finds \hat{p}^* that minimizes $\|\hat{p}\|$ subject to $B^T B\hat{p} = B^T f$. However, in tests with ground truth data we observe that the stresses found in this way do not always match that well (see Fig. 4). Thus, we use a radial basis function representation to regularize the reconstruction of stress correction through interpolation.

From each time step we have a set of principal stretches (and stretch rates) for each element. We assume that we always have a variety of deformations across elements and time (i.e., the principal stretches in the data we are fitting are not all the same). With k-means clustering, we select m stretches to use for interpolation, and define radial basis functions $\phi_i(\hat{F}) = \|\hat{F} - F_i\|$, for the cluster centers $i = 1, \dots, m$. Thus, we can write a smooth strain dependent stress correction as an RBF with m basis functions as

$$\Delta\hat{P} = \sum_{i=1}^m w_i \phi_i(\hat{F}) \quad (10)$$

where $w_i \in \mathbb{R}^3$ are the weights. For each time step i , we can assemble a tall matrix R_i containing the basis functions evaluated with \hat{F} for each element to write an equation for computing interpolated stress reconstructions,

$$\Delta\hat{p}_i = R_i w, \quad (11)$$

where the unknown weights are assembled here into a block vector w . These corrections must explain the gentle forces of Equation 5, but must also include the current parametric material stress correction Δp_c , that is,

$$f_i = B(R_i w - \Delta p_c). \quad (12)$$

Without a damping correction, we would solve for the weights with least squares using the above equation at all time steps. But we include a damping correction through a strain dependent modification of the Rayleigh parameter α_1 , thus, the above equation becomes

$$f_i = B(R_i w - \Delta p) + \left(\sum_j (R_{ij} w_{\alpha_1} - \Delta \alpha_{1c_j}) K_j \right) \dot{x}, \quad (13)$$

where K_j is the contribution of element j to the element stiffness matrix with its current strain, $\Delta \alpha_{1c_j}$ is the current Rayleigh correction for this element, and w_{α_1} are the weights for computing the new Rayleigh correction with R_{ij} being row j of matrix R_i . By least squares we solve for w and w_{α_1} simultaneously using the data from all time steps. Comparing with the method of [8], which explicitly interpolates the Young's modulus and Possion ratio using RBF functions, we directly interpolate the relationship between strain and stress. For the damping contribution, however, we use the same strategy of interpolating physical parameters.

6.2 Network Based Representation

The RBF correction provides a smooth parametric material correction, but can also be expensive to compute if many basis functions are used. Thus, once the iterative material learning process has converged, we learn a general neural network representation for the diagonal Piola stress correction, $N(\hat{F}, \hat{F})$, as seen in Equation 1. The training data are straightforward to compute. We use the learned RBF parametric model and run many simulations while recording principal stretches and stretch rates of elements. During simulation, we also record for each element the total diagonal Piola stress correction which is equal to the RBF in Equation 10 plus a dissipation stress contribution computed from the $\Delta \alpha_1$ Rayleigh damping correction.

We use a network configuration with two hidden layers as shown in Fig. 5. The network has 6 inputs, they are principal stretch and its rate, the output is the 3 dimensional stress correction (total of elastic and damping stresses). We use 6 nodes in each hidden layer. Having tested different activation functions with and without batch normalization, we have settled on using ELU activation functions [41] after a batch normalization layer [42] for better network performance and more robustness to noise. The evaluation can be seen in Fig. 6, where we used the same training data for all the network configurations, and the training data are generated from the first iteration output of the turtle example (see supplementary video).

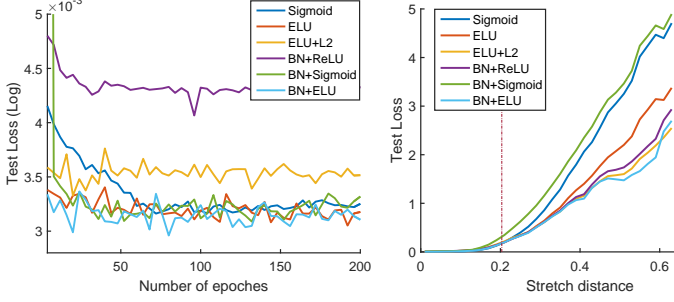


Fig. 6: Left, the network’s learning rate and test accuracy with different activation function configurations. Right, the network’s test accuracy along deformation scale of test data. We found that the combination of a Batch normalization layer + ELU has superior performance and robustness.

As the left plot in Fig. 6 shows, most of the activation function configurations, except for BN+ReLU, exhibit similar performance on learning speed and accuracy when the test data has similar deformation scale as the training data. Here we use the distance between principal stretch \hat{F} and non-deformed principal stretch $(1, 1, 1)$ to evaluate the deformation scale as $\|\hat{F} - (1, 1, 1)\|$. To show the ability of a network to extrapolate, we tested the network with much larger scales of deformation data, which can be seen in the plot at right of Fig. 6, where the training data resides in the left side of red dot line, in the range of $[0, 0.26]$. Beyond this range, ELU performs better than the sigmoid function.

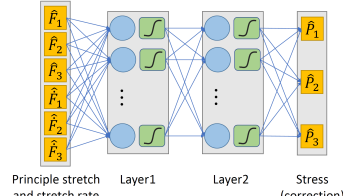


Fig. 5: Neural network configuration.

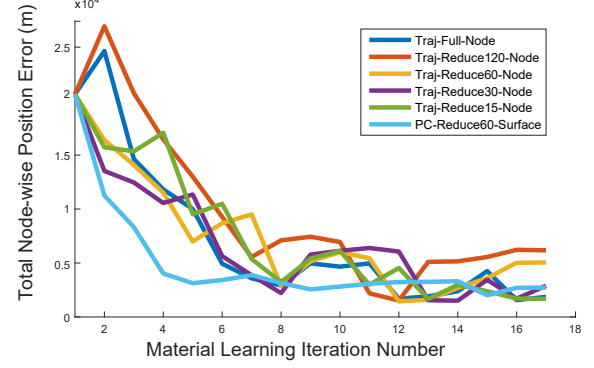


Fig. 7: Convergence comparison for learning a material correction with different space-time optimization strategies. Input is either synthetic surface trajectories ('Traj') or synthetic point cloud sequence ('PC'). Keywords 'Full' and 'Reduce μ ' distinguish between full and reduced space optimization, where μ is the number of basis functions.

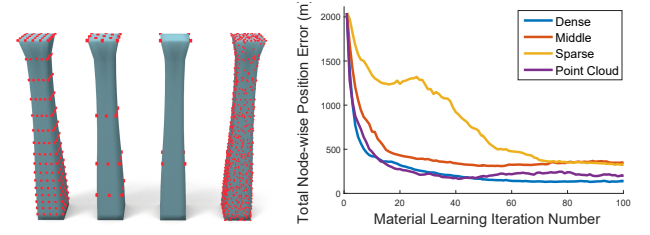


Fig. 8: Convergence comparison under different observation conditions. A neo-Hookean material with edited compression regions is the learning target. From left to right, 100%, 13%, and 6% of the surface nodes are assumed visible. Red dots indicate the exact location of visible nodes. The rightmost bar imitates a real application where the surface information is represented as point cloud data. The error norms in nodal positions are plotted on the right with different colors. They all converge sufficiently well.

first 5 curves in Fig. 7, node-wise position constraints lead to large control forces during the first several learning iterations, when the nominal material is far from ground truth. Consequently, this introduces some overshooting. Through reduced space-time optimization, these inconveniently large force residuals are smoothly distributed throughout the entire object’s domain. We observe good convergence as seen in the last curve in Fig. 7 for learning from point cloud trajectories.

Our algorithm can handle noisy and sparse observations. We tested it on the same synthetic examples with different observation conditions. The learning target is a neo-Hookean material with edited compression regions. Notice that in Fig. 8, the number of observation points in the first three cases drops sharply. For all these experiments, our algorithm can converge to a sufficiently accurate solution. We also used virtual scans to imitate a real capture situation, where point cloud data cover the whole surface. Our patch based position constraint adopted in the last case (Section 5.3) performs better than the sparse observation case and only mildly worse than the accurate full surface observation case.

7 RESULTS AND DISCUSSION

In the following sections, we describe experiments that help reveal what is taking place in each step of the algorithm. To validate the accuracy of our algorithm, we use both real captured data and synthetic data generated by forward simulations with known material properties.

7.1 Space-Time Optimization

Space-time optimization is the critical step in the entire pipeline to get training sets from pure kinematic trajectories. For this section we designed three tests using synthetic data to illustrate how our space-time optimization scheme can lead to the convergence of the entire algorithm. To better reflect real captured data in this evaluation, we also use virtual scans as input trajectories.

For a large scale system or a long trajectory, we must solve space-time optimization in reduced space. We test different space-time optimization strategies using the same synthetic example (turtle with neo-Hookean material) and compare how well they converge. The results are shown in Fig. 7. Tests using node based position constraints or point cloud patch based position constraints are distinguished by keyword ‘Node’ and ‘Surface’. From the comparison of the

TABLE 1: Statistics measured for different test cases. From left to right, the test object, the ground-truth constitutive material model, Young's modulus E_G , Poisson's ratio ν_G , Rayleigh damping parameters α_{0G} and α_{1G} for ground-truth material, nominal material type, the Young's modulus E_N , Poisson ratio ν_N , Rayleigh damping parameters α_{0N} and α_{1N} used for nominal model, and maximum position error for testing data reconstruction (for real data this term is the maximum position error for training data reconstruction). All the Young modulus values are in MPa and all the maximum position errors are measured using percentage of object size. All examples use a time step of 0.001 seconds. The letter U denotes user designed, letter R denotes real materials.

Case	Material (GT)	E_G	ν_G	α_{0G}	α_{1G}	Material (N)	E_N	ν_N	α_{0N}	α_{1N}	err_L
Turtle	neo-Hookean	2e4	0.43	0.0	0.0	Corotation	3.5e4	0.43	0.0	0.0	2.8
Dragon	StVK	1e5	0.40	0.0	0.0	Corotation	1.2e5	0.40	0.0	0.0	0.4
Sphere1	neo-Hookean (tension)	U	U	0	0.2	Corotation	1.2e5	0.43	0.0	0.2	4.1
Sphere2	neo-Hookean (compression)	U	U	0	0.2	Corotation	1.2e5	0.43	0.0	0.2	6.0
Bar (Damping1)	Corotation + strain-dep damping	4e4	0.43	U	0.2	Corotation	4e4	0.43	0.0	0.2	0.1
Bar (Damping2)	Corotation + strain-dep damping	4e4	0.43	U	0.2	Corotation	4e4	0.43	0.0	0.2	0.8
Pot Holder	Real Material	R	R	R	R	Corotation	2.4e6	0.43	0.0	0.0	3.0/7.0
Hanger	Real Material	R	R	R	R	Corotation	4.5e5	0.43	0.001	1.0	4.0
Silicon Bar	Real Material	R	R	R	R	Corotation	3.0e5	0.45	0	0.0	6.0
Bar (Heterogenous)	Corotation	1e5/1e7	0.40	0.0	0.0	Corotation	3e6	0.40	0.0	0.0	0.2/0.5

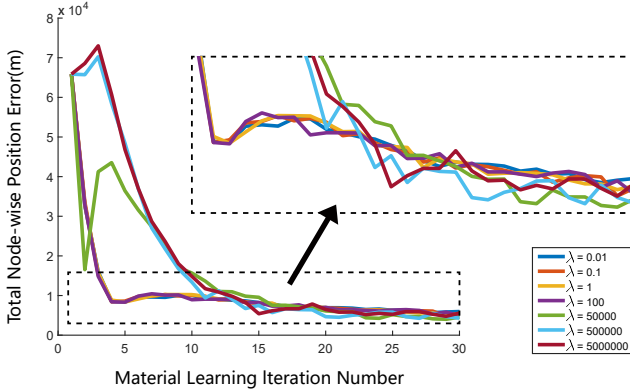


Fig. 9: Convergence comparison with different position constraint enforcement weights λ in Eq. (4). A neo-Hookean material with edited compression regions is the learning target. Seven significantly different values are selected, and the position error norms along learning iteration are plotted. Note that strong position constraints introduce vibration at early iterations, while soft ones mildly sacrifice accuracy.

As described in Equation 4, λ controls the enforcement strength of position constraints, which influences the control force. We chose different λ values in the wide range $[0.01, 500000]$, and simulated the same example (turtle with neo-Hookean material as learning target, all surface nodes assumed visible). From Fig. 9, we observe that larger λ introduce some vibration or even overshooting at the early optimization stages. The unbalanced ratio between force residual constraint and position constraint causes a large force deviation in the internal points, which consequently decreases the quality of generated training data. In contrast,

the curves corresponding to smaller λ are much smoother along the optimization iteration axis. From a global perspective, different λ will not necessarily produce significantly different final results, even though there are still subtle accuracy drops for smaller λ cases as illustrated in zoom-in of Fig. 9. We expect it should be possible to adaptively tune λ between iterations to speed up convergence. For real captured data, λ is chosen to be small, depending on the confidence in the observations.

7.2 Nonlinear Constitutive Material Modelling

To validate the generality of our parametric material model estimation algorithm, we test its ability to learn a variety of different materials using a co-rotational model for the nominal material. Ground truth trajectories are either generated in the VEGAfem [43] library using classical hyperelastic material model, or they are user defined elasticity and damping models, or captured by Kinect sensors. Table 1 shows the statistics of all our testing cases. Qualitative results for these cases can be seen in the supplementary video. Each case is discussed below, while reconstruction errors are listed in the last column of Table 1.

7.2.1 Classical Hyperelastic Material

The turtle (see Fig. 1) is made of neo-Hookean material; the dragon is made of StVK material. We use two deliberately designed test trajectories to validate our learning result. The first test has a similar deformation scale as the training trajectory, while the second test has a much larger range of deformation. Table 1 and the supplementary video show that the learning result can reproduce similar deformation

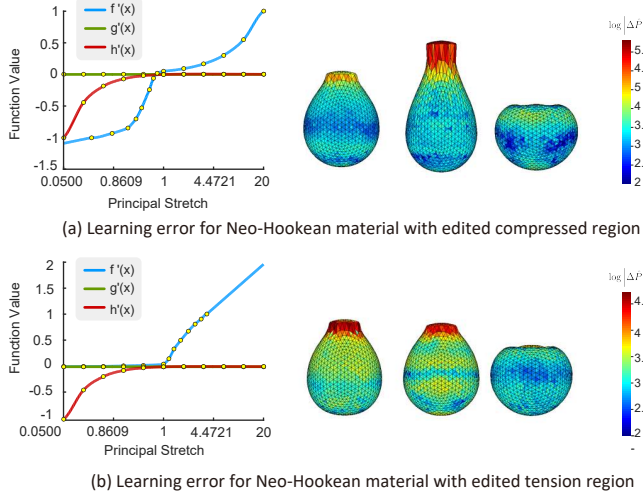


Fig. 10: Visualization of the learning result accuracy for user designed elastic material examples [2]. At left the plot shows edited compression and tension regions of a Neo-Hookean material. At right, the color illustrates principal stress error distribution of our learned parametric material correction to a corotational model.

with high accuracy; the results for different deformations also demonstrate low error. Vibration differences can only be observed towards the end of a sequence, and as such, can largely be attributed to error accumulation.

7.2.2 User Designed Elasticity and Damping Model

Our algorithm can be also extended to model user designed nonlinear elasticity and damping material models. Our third example is a soft solid sphere whose top part is keyframed in an up-down motion (Fig. 10). Following the method of [2], the internal elastic forces and tangent stiffness matrices are formulated in a polynomial space of principal stretch. Customized materials are designed by editing a single stress-strain curve using a spline interface. We tested two different designed nonlinear materials which edit tension and compression starting from the a neo-Hookean material as shown in Fig. 10. The supplementary video shows indistinguishable simulation trajectories, while Fig. 10 shows small stress reconstruction errors produced by our parametric material correction of a nominal corotational model. We also compared with the parameter fitting based method of [14] and a modification of the method which replaces the simple corotated elasticity model with a neo-Hookean model. The reported side by side comparison in Fig. 11 and the supplementary video both demonstrate that our method is superior to this parameter fitting algorithm, especially when the default model is simple.

Although linear viscous damping is widely used in the computer graphics community, this only constitutes a small subset of all viscous damping models. Under many circumstances, the damping matrix C can depend nonlinearly on both deformation and velocity. To validate the accommodation of our material model estimation algorithm for damping compensation, Fig. 12 shows our tests on a strain-dependent damping model. We start from a Rayleigh damping model, and substitute the original constant stiffness damping coefficient α_1 with a polynomial function of

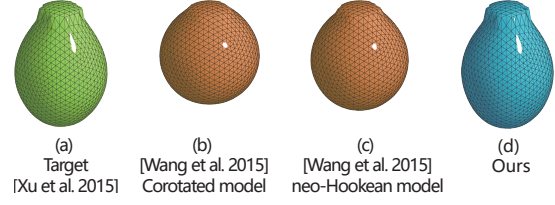


Fig. 11: Comparison with [14] on a user designed material learning example. From left to right, (a) target trajectory generated using neo-Hookean material with modified compressed region using the spline interface from [2]; (b) using [14]; (c) using an enhanced method for [14] that replaces the corotated model with the neo-Hookean model; and (d) using our algorithm.

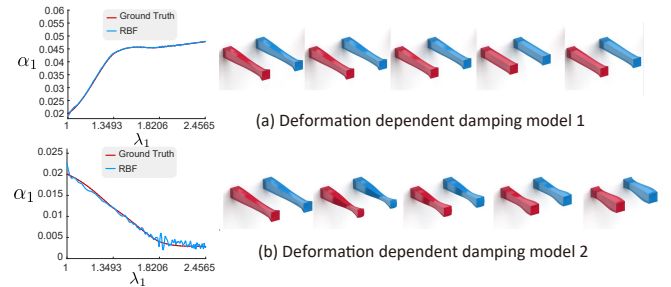


Fig. 12: Visualization of the learning result accuracy for user designed deformation dependent damping models. Red is used to show ground truth, while blue shows simulated poses with a learned parametric material correction.

the first principal stretch λ_1 . The function of deformation dependent α_1 is controlled using a spline tool.

Since our parametric material correction model is independent of topology, it can be easily transferred to other simulation scenarios. The neo-Hookean material with modified tension region model which we learned from ball example can be transferred, for example, to a chubby bunny. As can be gleaned from the video and Fig. 13(a), the bunny belly vibrates in a lively fashion during jumps. We also transfer the two deformation dependent damping models of Fig. 12 to different leaves of a taro plant to assign separate properties for young and old leaves as shown in the video and Fig. 13(b).

7.2.3 Real Material Fitting

We first validate our algorithm on a silicon bar example. The object is made by casting an elastomer material of type Silicon-601 into a bar-shaped mold. The target material properties depend on the amount of added curing agent, which has no default nominal value. Moreover, the numerous small air bubbles seen in Fig. 14(d) add more variance to the material properties. Thus, in the presence of these bubbles, it is worthwhile to allow an algorithm like ours to infer the material properties. As illustrated in Fig. 14(a) through (c), the object is fixed at one end, and three different external loads (100 g, 200 g, and 300 g) are added at the free end. We released the load and recorded its vibration. The trajectory of the 300 g case is used as training data, while the other two are used for testing. We learn

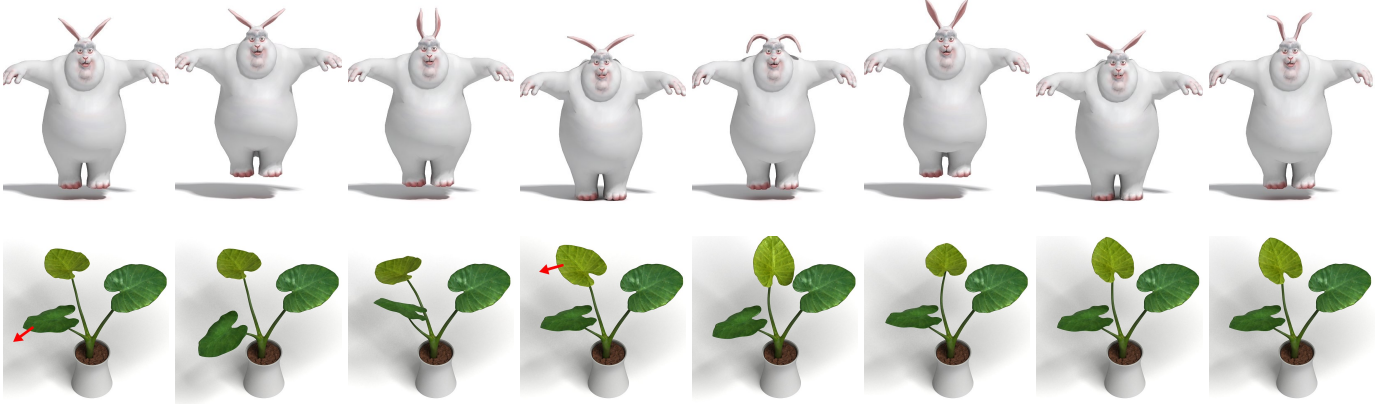


Fig. 13: Top: A chubby jumping bunny using the learned parametric material of the ball example designed material with modified tension region. Second row: A taro plant responds to user interactions. The left young leaf has damping property learned from the top deformation dependent damping model of Fig. 12; while the middle older leaf has damping property learned from the second deformation dependent damping model.

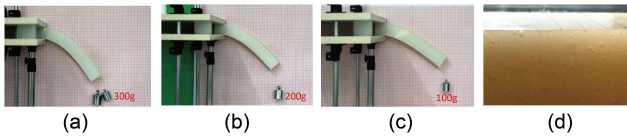


Fig. 14: Silicon bar examples: (a) 300 g external loading case is used as training data, (b) 200 g external loading case, and (c) 100 g external loading case are used as test data; (d) irregular bubbles can be observed in a magnified view.

the material using both our method and the method of [14]. We encourage the readers to watch the side by side comparison in the accompanying video.

We also validated and compared our algorithm with [14] for the real silicon pot holder and hanger examples, which are shown in Figs. 15 and 16, respectively. The captured trajectories seen in (a) of both figures are used to obtain material corrections. The raw point cloud data are fused, and severe outliers are removed using Artec Studio. The results are validated through external loading tests. More specifically, we fix the objects on one end, either horizontally or vertically, and attach different weights on the other end. The external weights are suddenly released and the vibrations of the soft object are simulated and compared with the ground truth. A side by side comparison can be seen in the accompanying video. For the hanger and silicon bar example, we observed that the original constant mass damping coefficient α_0 must be substituted with a polynomial function of principal stretch λ .

7.3 Material Coarsening

The algorithm proposed in this paper can also be used for material coarsening. In Fig. 17, a high resolution bar ($8 \times 8 \times 34$) is composed of two different constitutive materials, with Young modulus values of $1e5$ and $1e7$, respectively. The two materials are composed in a layer by layer manner, represented by the light and dark green colors. The low resolution mesh is the result of coarsening by factor 2 along three axis directions. Two principal defor-

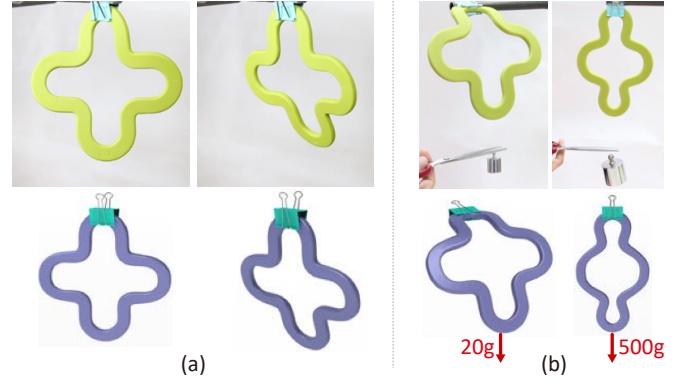


Fig. 15: Real Material Fitting: (a) Two captured trajectories and the corresponding tracking result. (b) Static loading tests: a silicon pot holder is bent and pulled by external weights; the holder is fixed at one end horizontally and vertically.

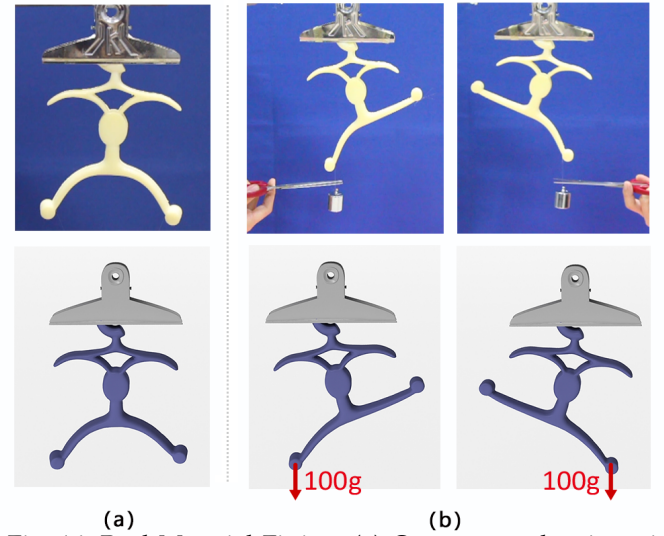


Fig. 16: Real Material Fitting: (a) One captured trajectories and the corresponding tracking result. (b) Static loading tests: a silicon hanger is pulled by external weights; the hanger is fixed at top vertically.

TABLE 2: Performance statistics measured for different testing cases. Listed from left to right are the test object, number of vertices, number of tet elements, number of frames for training data, number of reduced modes, number of learning iterations, number of RBF kernels, and total computation time for material learning. The computation times are in hours.

Case	#vert	#tet	#frm	#mode	#iter	#kernel	CPU
Turtle	347	1185	400	200	29	46	0.9
Dragon	959	2590	400	200	19	140	1.1
Sphere 1	2655	12712	400	200	27	140	9.1
Sphere 2	2655	12712	400	200	23	140	7.7
Bar (Damp1)	425	1536	300	150	7	400	0.4
Bar (Damp2)	425	1536	800	400	18	500	2.5
Pot Holder	3031	8843	400	200	10	140	4.2
Hanger	1740	5888	375	200	4	500	2
Silicon Bar	650	2400	600	full	6	300	0.5

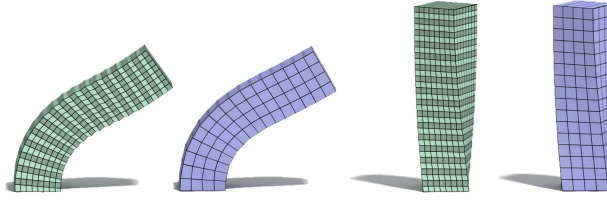


Fig. 17: Material coarsening. The green bar shows the fine mesh with a layered material distribution; the purple bar is the corresponding coarsened mesh with homogeneous material distribution. Bend (left) and twist (right) deformation trajectories of fine mesh are used as training data, and the purple bars are the reconstruction result after learning.

mation modes (bend and twist) are used as training data. The equivalent coarsened material property found by our algorithm can produce very similar motion to the original high resolution heterogeneous model.

7.4 Comparing RBF and NN Representations

In our algorithm, we use two parametric material representations. The RBF based representation is used during iterative material learning while the NN representation is trained after the material correction is achieved. We follow standard practices in training our networks, computing scaling factors for the inputs and outputs based on the training data so that both inputs and outputs have zero mean and unit variance. We randomly permute the order of the samples across time to improve training.

Fig. 19 shows the generality of both types of parametric representations. We choose NN, RBF, and RBF augmented with a low-order polynomial as candidates. Each row of Fig.19 corresponds to one scenario. The top row has larger test data distribution (blue dots in (a)) than training data (red dots in (a)). All three representations perform well in the range where the deformations are covered by training data. The performance of both NN and RBF with polynomial drops severely when the deformation is out of the range of the training data. In the bottom row, when a sparse set of additional training data is included (pink dots in (e)),

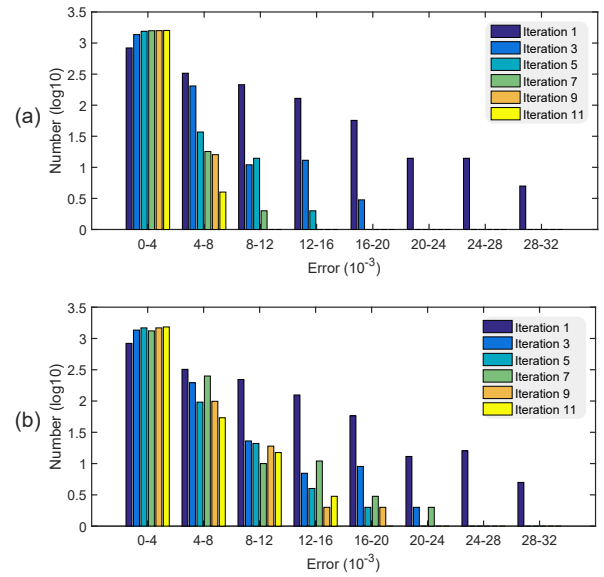


Fig. 18: Comparison of convergence stability showing histograms of error sizes with increasing learning iterations, (a) using RBF based representation, the number of position errors (forward simulation with material correction compared to ground truth) in all bins decrease rapidly, except for the smallest errors ($4e-3$ and smaller), (b) when using a neural network representation in the learning method, the error reduction is slower.

the performance for all representations improves greatly. The generality of the different representations is highly dependent on data, especially for complex highly nonlinear target materials such as the neo-Hookean material with edited tension region that we used here. Since the material is edited in a piece-wise manner, the training data must cover the entire working space in order to recover the material faithfully.

Fig. 20 shows that NN training using data that comes from simulation sequences leads to unfaithful stress reconstructions as visualized by their isosurfaces in comparison to ground truth. In contrast, the isosurfaces visualized for the RBF based representation are close to the required

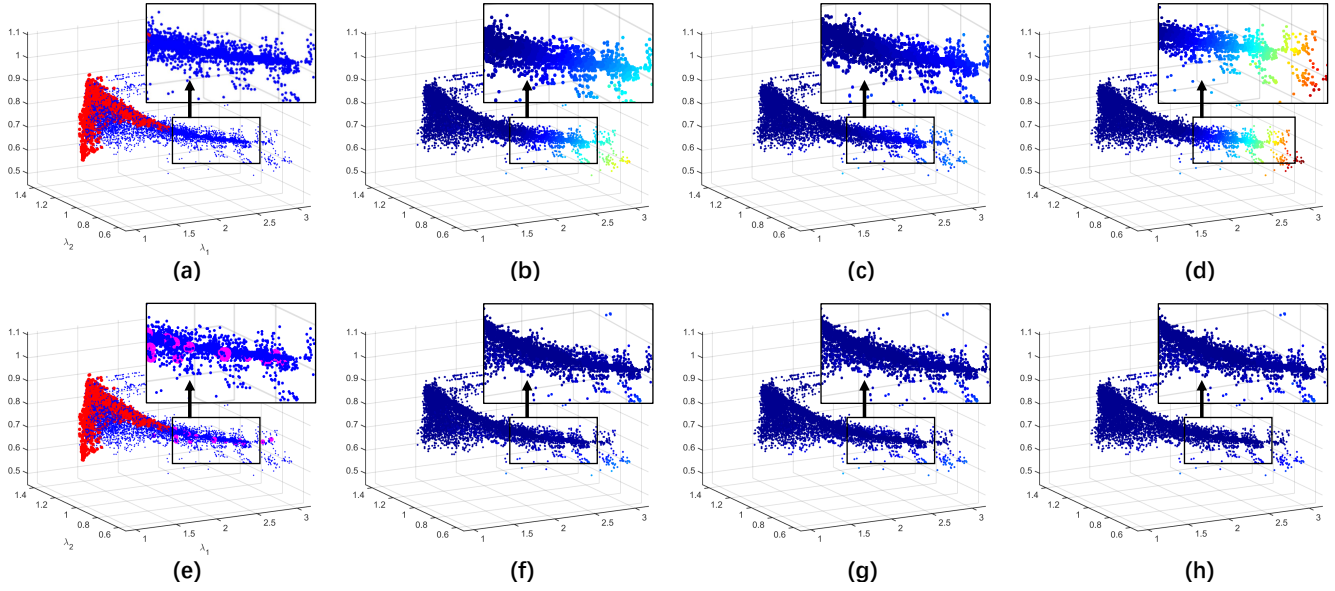


Fig. 19: Generality comparison of parametric representations. Each row corresponds to one specific training data configuration. The first column illustrates the distribution of training (red dots) and test data (blue dots). The pink dots in first column represent additional sparse training data. The second, third and fourth columns are the result of NN, RBF, and RBF with polynomial's result respectively, where the Matlab jet colour map is used to indicate the magnitude of the error.

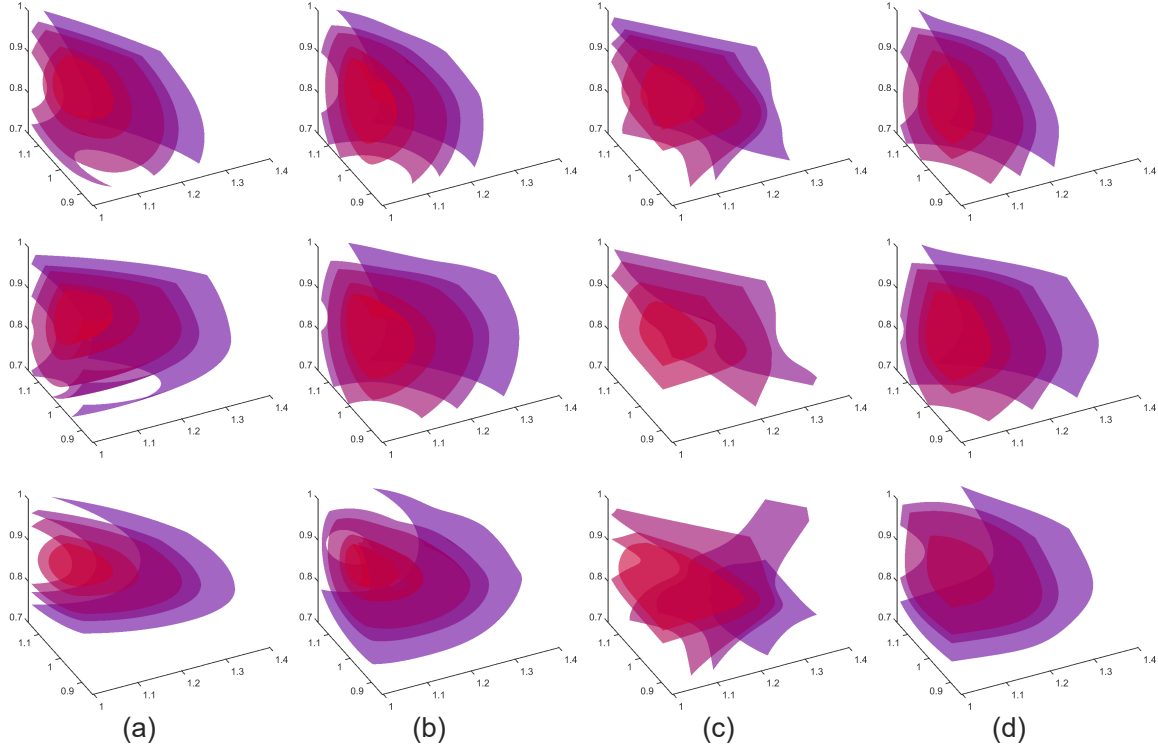


Fig. 20: Comparison on function learning result between two parametric material models. The plots show isosurfaces of the parametric material model for different components (each row shows one component of the principal stress). (a) ground truth, (b) RBF based representation, (c) NN direct learning result, and (d) NN learning result for fitting the RBF.

ground truth correction. Because we can generate much more training data through evaluation of our RBF representation, this leads to a faithful neural network based representation which is also less expensive to compute. Fig. 18 shows statistics on the distribution of position errors (comparing forward simulation with material correction to ground truth) with increasing learning iterations. Using the

RBF based representation, the number of larger position errors decrease faster with fewer iterations than the errors tabulated for an iterative learning process that uses a network model throughout.

7.5 Performance

We measured the computational cost for each critical step on a 10-core 3.0 GHz Intel i7-6950X desktop. The performance for space-time optimization, listed in Table 2, correlates with the number of tetrahedral elements, the number of frames in the motion trajectory, the number of RBF kernels, and number of selected reduced basis. We also performed a quantitative comparison regarding the computation time for RBF and NN parametric representations. In our test, the RBF representation had 100 kernels, while the NN had the structure illustrated in Fig. 5. The amount of testing data varied in the range [200, 20000] with steps of 200. According to our statistics, the computation time of NN evaluation is constantly 3 times faster than RBF evaluation under this configuration.

8 CONCLUSION AND FUTURE WORK

We have presented a new method for estimating nonlinear constitutive models from trajectories of surface data. The key insight is to have a parametric material correction model learn the error of the elastic and damping properties of a nominal material. A framework for gradually learning this correction from only kinematic data is described. We have demonstrated our method with several examples, illustrating the ability of our approach to learn classical material models, user designed materials (cartoon physics), and real world captured data.

The desire to work with realistic constitutive models when simulating complex motion has been shared for a long while by researchers from many fields, not just computer graphics. The possibility of employing machine learning technology towards such a goal is tantalizing. Although our current framework only employs neural network technology as a compression tool, we solved an interesting and timely problem which is critical for all machine learning algorithms for generating annotated data automatically. We believe our present work is an important step in that direction.

There are a number of interesting ideas to explore in future research. First, we note that extending our approach to accommodate a variety of numerical integration techniques would help in avoiding or reducing step size dependent numerical damping effects in our results. Second, we only address heterogeneous materials in the case of numerical coarsening to a homogeneous material. There are interesting extensions that can be considered for dealing with varying material properties across a model, for instance, by adding a latent material parameter to our representation. Finally, there are still a variety of potential damping effects that we cannot capture with our approach. The models we estimate do not account for any hysteresis in the damping model, while this can be common in real materials, as can also be the presence of plastic deformation. Capturing a larger variety of complex plastic and damping behaviors is indeed a very interesting avenue for future work.

REFERENCES

- [1] H. Xu and J. Barbić, "Example-based damping design," *ACM Trans. Graph.*, vol. 36, no. 4, pp. 53:1–53:14, Jul. 2017. [Online]. Available: <http://doi.acm.org/10.1145/3072959.3073631>
- [2] H. Xu, F. Sin, Y. Zhu, and J. Barbić, "Nonlinear material design using principal stretches," *ACM Trans. Graph.*, vol. 34, no. 4, pp. 75:1–75:11, Jul. 2015. [Online]. Available: <http://doi.acm.org/10.1145/2766917>
- [3] D. K. Pai, K. v. d. Doel, D. L. James, J. Lang, J. E. Lloyd, J. L. Richmond, and S. H. Yau, "Scanning physical interaction behavior of 3d objects," in *Proc. of SIGGRAPH*, 2001, pp. 87–96.
- [4] J. Schöner, J. Lang, and H.-P. Seidel, "Measurement-based interactive simulation of viscoelastic solids," *Computer Graphics Forum*, vol. 23, no. 3, pp. 547–556, 2004.
- [5] M. Becker and M. Teschner, "Robust and efficient estimation of elasticity parameters using the linear finite element method," in *Proc. Simulation und Visualization*, 2007, pp. 15–28.
- [6] H. Wang, J. F. O'Brien, and R. Ramamoorthi, "Data-driven elastic models for cloth: Modeling and measurement," *ACM Trans. on Graphics*, vol. 30, no. 4, pp. 71:1–71:12, 2011.
- [7] E. Miguel, D. Bradley, B. Thomaszewski, B. Bickel, W. Matusik, M. A. Otaduy, and S. Marschner, "Data-driven estimation of cloth simulation models," *Computer Graphics Forum*, vol. 31, no. 2, pp. 519–528, 2012.
- [8] B. Bickel, M. Bächer, M. A. Otaduy, W. Matusik, H. Pfister, and M. Gross, "Capture and modeling of non-linear heterogeneous soft tissue," *ACM Trans. on Graphics*, vol. 28, no. 3, pp. 89:1–89:9, 2009.
- [9] E. Miguel, R. Tamstorf, D. Bradley, S. C. Schwartzman, B. Thomaszewski, B. Bickel, W. Matusik, S. Marschner, and M. A. Otaduy, "Modeling and estimation of internal friction in cloth," *ACM Trans. Graph.*, vol. 32, no. 6, pp. 212:1–212:10, Nov. 2013. [Online]. Available: <http://doi.acm.org/10.1145/2508363.2508389>
- [10] E. Miguel, D. Miraut, and M. A. Otaduy, "Modeling and estimation of energy-based hyperelastic objects," *Computer Graphics Forum*, vol. 35, no. 2, pp. 385–396, 2016. [Online]. Available: <http://dx.doi.org/10.1111/cgf.12840>
- [11] K. S. Bhat, C. D. Twigg, J. K. Hodgins, P. K. Khosla, Z. Popović, and S. M. Seitz, "Estimating cloth simulation parameters from video," in *Proc. ACM SIGGRAPH/Eurographics Symp. on Computer Animation*, 2003, pp. 37–51.
- [12] S. Yang, J. Liang, and M. C. Lin, "Learning-based cloth material recovery from video," in *The IEEE International Conference on Computer Vision (ICCV)*, Oct 2017.
- [13] A. Davis, K. L. Bouman, J. G. Chen, M. Rubinstein, O. Büyüköztürk, F. Durand, and W. T. Freeman, "Visual vibrometry: Estimating material properties from small motions in video," *IEEE Trans. Pattern Analysis & Machine Intelligence*, vol. 39, no. 4, pp. 732–745, 2017.
- [14] B. Wang, L. Wu, K. Yin, U. Ascher, L. Liu, and H. Huang, "Deformation capture and modeling of soft objects," *ACM Trans. Graph.*, vol. 34, no. 4, pp. 94:1–94:12, Jul. 2015. [Online]. Available: <http://doi.acm.org/10.1145/2766911>
- [15] S. Martin, B. Thomaszewski, E. Grinspun, and M. Gross, "Example-based elastic materials," *ACM Trans. Graph.*, vol. 30, no. 4, pp. 72:1–72:8, 2011.
- [16] C. Schumacher, B. Thomaszewski, S. Coros, S. Martin, R. Sumner, and M. Gross, "Efficient simulation of example-based materials," in *Proc. ACM SIGGRAPH/Eurographics Symp. on Computer Animation*, 2012.
- [17] D. Chen, D. I. W. Levin, S. Sueda, and W. Matusik, "Data-driven finite elements for geometry and material design," *ACM Trans. Graph.*, vol. 34, no. 4, pp. 74:1–74:10, Jul. 2015. [Online]. Available: <http://doi.acm.org/10.1145/2766889>
- [18] J. Panetta, Q. Zhou, L. Malomo, N. Pietroni, P. Cignoni, and D. Zorin, "Elastic textures for additive fabrication," *ACM Trans. Graph.*, vol. 34, no. 4, pp. 135:1–135:12, Jul. 2015. [Online]. Available: <http://doi.acm.org/10.1145/2766937>
- [19] D. Chen, D. I. W. Levin, W. Matusik, and D. M. Kaufman, "Dynamics-aware numerical coarsening for fabrication design," *ACM Trans. Graph.*, vol. 36, no. 4, pp. 84:1–84:15, Jul. 2017. [Online]. Available: <http://doi.acm.org/10.1145/3072959.3073669>
- [20] L. Kharevych, P. Mullen, H. Owhadi, and M. Desbrun, "Numerical coarsening of inhomogeneous elastic materials," *ACM Trans. Graph.*, vol. 28, no. 3, pp. 51:1–51:8, Jul. 2009. [Online]. Available: <http://doi.acm.org/10.1145/1531326.1531357>
- [21] M. Nesme, P. G. Kry, L. Jeřábková, and F. Faure, "Preserving topology and elasticity for embedded deformable models," in *ACM SIGGRAPH 2009 Papers*, ser. SIGGRAPH '09. New York, NY, USA: ACM, 2009, pp. 52:1–52:9. [Online]. Available: <http://doi.acm.org/10.1145/1576246.1531358>

[22] R. Torres, A. Rodríguez, J. M. Espadero, and M. A. Otraduy, "High-resolution interaction with corotational coarsening models," *ACM Trans. Graph.*, vol. 35, no. 6, pp. 211:1–211:11, Nov. 2016. [Online]. Available: <http://doi.acm.org/10.1145/2980179.2982414>

[23] R. M. Sánchez-Banderas and M. A. Otraduy, "Strain rate dissipation for elastic deformations," *Computer Graphics Forum*, vol. 37, no. 8, pp. 161–170, 2018.

[24] J. Ghaboussi, J. Garrett Jr, and X. Wu, "Knowledge-based modeling of material behavior with neural networks," *Journal of Engineering Mechanics*, vol. 117, no. 1, pp. 132–153, 1991.

[25] J. Ghaboussi, D. A. Pecknold, M. Zhang, and R. M. Haj-Ali, "Autoprogessive training of neural network constitutive models," *International Journal for Numerical Methods in Engineering*, vol. 42, no. 1, pp. 105–126, 1998.

[26] S. Jung and J. Ghaboussi, "Neural network constitutive model for rate-dependent materials," *Computers & Structures*, vol. 84, no. 15, pp. 955 – 963, 2006.

[27] D. Stefanos and P. Gyan, "On neural network constitutive models for geomaterials," *Journal of Civil Engineering Research*, vol. 5, no. 5, pp. 106–113, 2015.

[28] L. Liang, L. Minliang, and S. Wei, "A deep learning approach to estimate chemically-treated collagenous tissue nonlinear anisotropic stress-strain responses from microscopy images," *Acta Biomaterialia*, vol. 63, no. Supplement C, pp. 227 – 235, 2017.

[29] R. Luo, T. Shao, H. Wang, W. Xu, X. Chen, K. Zhou, and Y. Yang, "Nnwarp: Neural network-based nonlinear deformation," *IEEE Trans. Visualization & Computer Graphics*, 2018.

[30] L. Fulton, V. Modi, D. Duvenaud, D. I. W. Levin, and A. Jacobson, "Latent-space dynamics for reduced deformable simulation," *Computer Graphics Forum*, 2019.

[31] E. Sifakis and J. Barbic, "FEM simulation of 3D deformable solids: A practitioner's guide to theory, discretization and model reduction," in *ACM SIGGRAPH 2012 Courses*, ser. SIGGRAPH '12, 2012, pp. 20:1–20:50.

[32] G. Irving, J. Teran, and R. Fedkiw, "Invertible finite elements for robust simulation of large deformation," in *Proceedings of the 2004 ACM SIGGRAPH/Eurographics Symposium on Computer Animation*, ser. SCA '04. Aire-la-Ville, Switzerland, Switzerland: Eurographics Association, 2004, pp. 131–140. [Online]. Available: <http://dx.doi.org/10.1145/1028523.1028541>

[33] A. Witkin and M. Kass, "Spacetime constraints," in *Proceedings of the 15th Annual Conference on Computer Graphics and Interactive Techniques*, ser. SIGGRAPH '88. New York, NY, USA: ACM, 1988, pp. 159–168. [Online]. Available: <http://doi.acm.org/10.1145/54852.378507>

[34] J. Barbic, M. da Silva, and J. Popović, "Deformable object animation using reduced optimal control," *ACM Trans. Graph.*, vol. 28, no. 3, pp. 53:1–53:9, Jul. 2009. [Online]. Available: <http://doi.acm.org/10.1145/1531326.1531359>

[35] C. Schulz, C. von Tycowicz, H.-P. Seidel, and K. Hildebrandt, "Animating deformable objects using sparse spacetime constraints," *ACM Trans. Graph.*, vol. 33, no. 4, pp. 109:1–109:10, Jul. 2014. [Online]. Available: <http://doi.acm.org/10.1145/2601097.2601156>

[36] S. Dalton, N. Bell, L. Olson, and M. Garland, "Cusp: Generic parallel algorithms for sparse matrix and graph computations," 2014, version 0.5.0. [Online]. Available: <http://cusplibrary.github.io/>

[37] C. G. Petra, O. Schenk, M. Lubin, and K. Gärtner, "An augmented incomplete factorization approach for computing the Schur complement in stochastic optimization," *SIAM Journal on Scientific Computing*, vol. 36, no. 2, pp. C139–C162, 2014.

[38] C. G. Petra, O. Schenk, and M. Anitescu, "Real-time stochastic optimization of complex energy systems on high-performance computers," *IEEE Computing in Science & Engineering*, vol. 16, no. 5, pp. 32–42, 2014.

[39] J. Schulman, A. Lee, J. Ho, and P. Abbeel, "Tracking deformable objects with point clouds," in *Proc. IEEE Int. Conf. on Robotics & Automation*, 2013.

[40] C. C. Paige and M. A. Saunders, "LSQR: An algorithm for sparse linear equations and sparse least squares," *ACM Trans. Math. Softw.*, vol. 8, no. 1, pp. 43–71, Mar. 1982. [Online]. Available: <http://doi.acm.org/10.1145/355984.355989>

[41] D.-A. Clevert, T. Unterthiner, and S. Hochreiter, "Fast and accurate deep network learning by exponential linear units (elus)," *Computer Science*, 2015.

[42] S. Ioffe and C. Szegedy, "Batch normalization: Accelerating deep network training by reducing internal covariate shift," in *International Conference on International Conference on Machine Learning (ICML)*, 2015, pp. 448–456.

[43] J. Barbić, F. S. Sin, and D. Schroeder, "Vega FEM Library," 2012, <http://www.jernejbarbic.com/vega>.